catalysts

MDPI

Article

Oxygen-Vacancy-Rich Fe@Fe_3O_4 Boosting Fenton Chemistry

Rongwei Zheng [1,†], Ruifan Tan [2,†], Yali Lv [2], Xiaoling Mou [2,3,*], Junqiao Qian [1], Ronghe Lin [2,3], Ping Fang [4,*] and Weidong Kan [5]

1 Department of Hydraulic Engineering, Zhejiang Tongji Vocational College of Science and Technology, Hangzhou 311231, China; zjzrw0910@126.com (R.Z.); qianjunqiao@zjtjkjzyxy8.wecom.work (J.Q.)
2 Hangzhou Institute of Advanced Studies, Zhejiang Normal University, 1108 Gengwen Road, Hangzhou 311231, China; ruifan.tan@zjnu.edu.cn (R.T.); yalilv@zjnu.edu.cn (Y.L.); catalysis.lin@zjnu.edu.cn (R.L.)
3 Key Laboratory of the Ministry of Education for Advanced Catalysis Materials, Zhejiang Normal University, 688 Yingbin Road, Jinhua 321004, China
4 College of Chemistry and Chemical Engineering, Shaoxing University, Shaoxing 312000, China
5 Shandong Tsurumi Hongqi Environmental Technology Co., Ltd., Weifang 261108, China; wfhqwd@126.com
* Correspondence: xiaoling.mou@zjnu.edu.cn (X.M.); fangping@usx.edu.cn (P.F.)
† These authors contributed equally to this work.

Abstract: Iron-based materials are widely applied in Fenton chemistry, and they have promising prospects in the processing of wastewater. The composition complexity and rich chemistry of iron and/or oxides, however, hamper the precise understanding of the active sites and the working mechanism, which still remain highly controversial. Herein, iron oxides of four different model systems are designed through a conventional precipitation method plus H_2 reduction treatment. These systems feature Fe@Fe_3O_4 with abundant oxygen vacancy, Fe^0 and Fe_3O_4 particles with interface structures, and Fe_3O_4-dominated nanoparticles of different sizes. These materials are applied in the decomposition of methyl orange as a model reaction to assess the Fenton chemistry. The Fe@Fe_3O_4 with core–shell structures exhibits significantly higher decomposition activity than the other Fe_3O_4-rich nanoparticles. A thin Fe_3O_4 layer formed by auto-oxidation of iron particles when exposed to air can boost the activity as compared with the Fe^0 and Fe_3O_4 particles with interface structures but poor oxygen vacancy. The unique hetero-structure with the co-existence of both metallic iron and oxygen vacancy displays excellent redox propensity, which might account for the superior Fenton activity. This finding provides a new perspective to understand and design highly efficient iron-based Fenton catalysts.

Keywords: advanced oxidation process; core–shell structure; fenton chemistry; Fe@Fe_3O_4 interface; methyl orange decomposition; oxygen vacancy

Citation: Zheng, R.; Tan, R.; Lv, Y.; Mou, X.; Qian, J.; Lin, R.; Fang, P.; Kan, W. Oxygen-Vacancy-Rich Fe@Fe_3O_4 Boosting Fenton Chemistry. *Catalysts* **2023**, *13*, 1057. https://doi.org/10.3390/catal13071057

Academic Editor: Enric Brillas

Received: 25 May 2023
Revised: 19 June 2023
Accepted: 20 June 2023
Published: 30 June 2023

1. Introduction

The widespread pollution of wastewater due to the discharge of high-concentration chemical solutions containing diverse organic compounds from the industry has posed a formidable challenge to a sustainable society [1–4]. The conventional approaches to wastewater management relying on biodegradation or physiochemical methods (such as the combination of chlorination and adsorption) are still not optimal for handling industrial wastewater. In this context, advanced oxidation processes (AOPs) are catching great attention as one of the most promising alternative solutions [5–8]. Compared with the traditional biodegradation method, which might be subjected to biomass poisoning, AOPs are a non-selective technology that depends on the oxidation of organic compounds with the in situ generated radical species with a strong oxidizing ability. Therefore, it is extremely flexible in handling the diversity of organic pollutants from the different chemical sectors.

As one of the most cost-effective AOP technologies, the Fenton process has drawn great interest in wastewater treatment [5,6]. The classic Fenton chemistry is initiated by

the formation of hydroxyl radicals (HO*) through the activation of H_2O_2 by Fe^{2+} ions. The as-formed HO*, together with other radicals with strong oxidizing potentials, can then convert the organic pollutants into smaller molecules or CO_2 [6]. To further enhance the oxidation efficiency, similar Fenton-like processes, such as photo-Fenton [9–11], electro-Fenton [12], and sono-Fenton [13], have also been studied by different researchers. Despite the difference in various techniques, the development of highly active Fenton catalysts is of optimal importance. The classic Fenton reaction was performed by soluble iron salts as homogeneous catalysts conducted at an optimal pH of 3.0. In addition to the requirement of neutralization before the discharge, the precipitation and subsequent disposal of iron hydroxides are the major problems [8]. To overcome this disadvantage, different heterogeneous Fenton systems have been proposed, which can be roughly classified into two categories: (i) the iron-containing catalysts, including iron minerals, clay-based catalysts, and other iron-containing catalysts; and (ii) non-ferrous catalysts based on cerium [14], chromium [15], cobalt [16], copper [17], manganese [18], ruthenium [19], and polyoxometalates [20]. Despite extensive explorations, iron-based Fenton systems possess several advantages, such as the high reactivity of Fe^{2+}/Fe^{3+} [21], the abundance and low cost of the metal, and low toxicity and environmental compatibility, rendering them highly appealing.

Iron minerals, including magnetite (Fe_3O_4) [22–24], hematite (α-Fe_2O_3) [25], maghemite (γ-Fe_2O_3) [26], goethite (α-FeOOH) [27], akaganèite (β-FeOOH) [28,29], lepidocrocite (γ-FeOOH), etc., are among the most extensively studied Fenton systems. In addition, zero-valence iron (ZVI) [30–32] and hybridized structures (e.g., Fe@Fe_2O_3 [33–36] and Fe^{2+}/Fe@Fe_2O_3 [37,38]) are also widely explored. Despite the different compositions and structures of these catalytic materials, it is generally accepted that Fe^{2+} species are crucial for the generation of HO* [5–8]. However, highly controversial questions remain regarding the nature of the active sites for metallic iron and oxides. For instance, Yuan et al. [31] employed ZVI in methyl orange decomposition and found an activity drop in consecutive runs. Analysis of the recovered catalyst confirmed the formation of oxide layers that was suggested to be responsible for the activity degrading. On the contrary, recent studies showed that by combining ZVI with iron oxides such as Fe@Fe_2O_3 core–shell structures are able to achieve excellent Fenton activity [33]. It has been proposed that Fe^0 can transfer two electrons to O_2 to generate H_2O_2, which further reacts with generated Fe^{2+} to produce HO* under acidic to neutral pH conditions [36]. The above opposing opinions highlight the necessity of a more in-depth understanding of the Fe^0 and iron oxide interfaces. Furthermore, ZVI is known to be susceptible to auto-oxidation when exposed to air. This means the outermost surfaces of the bulk metallic iron are likely covered by iron oxide layers. The nature of these layers and the impact on the Fenton activity are still not well understood.

In this contribution, we synthesized different iron oxide-based model systems through a conventional precipitation method in conjunction with H_2 reduction treatment. These systems showed very different structural features: (1) Fe^0-rich cores covered with Fe_3O_4 layers (Fe@Fe_3O_4), (2) Fe^0 and Fe_3O_4 nanoparticles with interface structures, and (3) Fe_3O_4-dominated nanoparticles of different sizes. These materials were then applied as the Fenton catalysts in the decomposition of methyl orange, which was selected as the model reaction to assess the catalytic activity in the removal of azo-dye pollutants from aqueous solutions [39]. Our catalytic results showed that the first two systems with the co-existence of both Fe^0 and Fe_3O_4 phases were significantly more active than the Fe_3O_4-dominated nanoparticles of different sizes, and the Fe@Fe_3O_4 with core–shell structures exhibited more than twice higher decomposition activity than the Fe^0 and Fe_3O_4 nanoparticles with interface structures. We also demonstrated that a thin Fe_3O_4 layer up to tens of nanometers was formed by the auto-oxidation of iron particles when exposed to air, leading to similar core–shell structures of the Fe@Fe_3O_4 model system and, consequently, comparable Fenton activity. Furthermore, our results also indicated that the redox propensity might be a more critical activity descriptor than the contents of Fe^{2+} and oxygen vacancy in the Fenton chemistry, and the co-existence of both zero-valent iron and rich oxygen vacancy can boost the Fenton activity.

2. Results and Discussion

2.1. Synthesis and Characterization of the Iron Oxides

2.1.1. Synthesis of the Iron Oxides

Different iron oxides were prepared by the precipitation methods by varying the iron precursors and the surfactants (Figure 1). The resultant precipitates derived from $Fe(NH_4)_2(SO_4)_2{\cdot}6H_2O$, $Fe(NO_3)_3{\cdot}9H_2O$, and $FeCl_3{\cdot}6H_2O$ were denoted as Fe_2O_3–S–P, Fe_2O_3–N–E, and Fe_2O_3–Cl–P, respectively. These samples were further subject to H_2 reduction before the application in MO decomposition. In addition, a commercial sample denoted as Fe_3O_4–C was purchased as the reference.

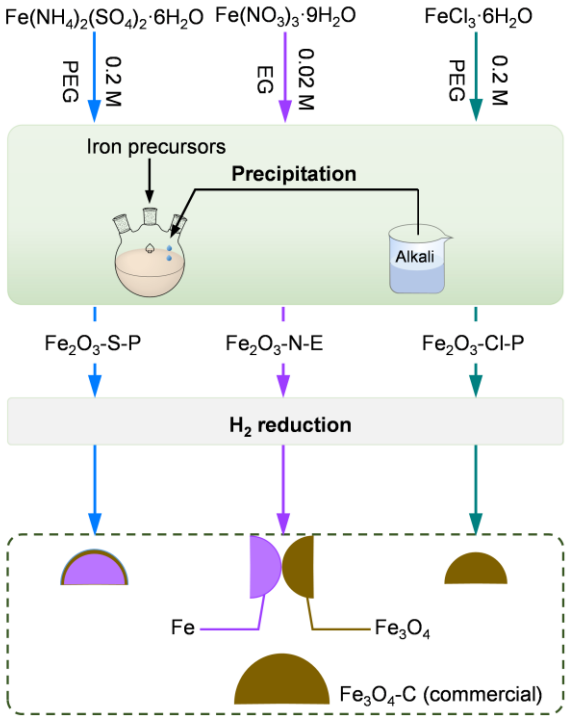

Figure 1. Schematic illustration of the synthetic procedures of the iron oxides, accompanied by the sample codes and structural characteristics.

2.1.2. Compositional and Structural Analyses of the Iron Oxides

The compositions of the as-prepared iron oxides were first checked by powder X-ray diffraction patterns (PXRD, Figure 2). The representative diffraction lines corresponding to α-Fe_2O_3 (PDF # 33-0664) can be found for all the samples, confirming the successful synthesis of the targeted materials. In addition, these materials showed clear differences in the diffraction intensities with the order of Fe_2O_3–Cl–P ~ Fe_2O_3–N–E >> Fe_2O_3–S–P. The crystallite sizes of Fe_2O_3 were then estimated by using the Scherrer equation and the (104) facet. The sizes of Fe_2O_3–Cl–P, Fe_2O_3–N–E, and Fe_2O_3–S–P were determined to be 44, 33, and 15 nm, respectively. The morphologies of as-derived Fe_2O_3 were studied by combined electron microscopic techniques (Figure 3). Scanning electron microscopy (SEM) revealed the formation of condensed aggregates for Fe_2O_3–S–P and Fe_2O_3–N–E and the more homogeneous nanospheres for Fe_2O_3–Cl–P, which were likely resulting from the combined use of different iron precursors and surfactants. In line with the SEM observation, transmission electron microscopy (TEM) also confirmed the relatively smaller sizes of the irregular nanoparticles for Fe_2O_3–S–P and Fe_2O_3–N–E.

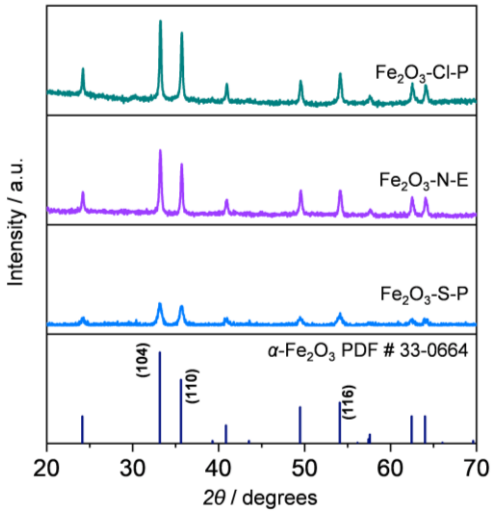

Figure 2. The PXRD patterns of the as-prepared iron oxides. Vertical lines are the reference standard.

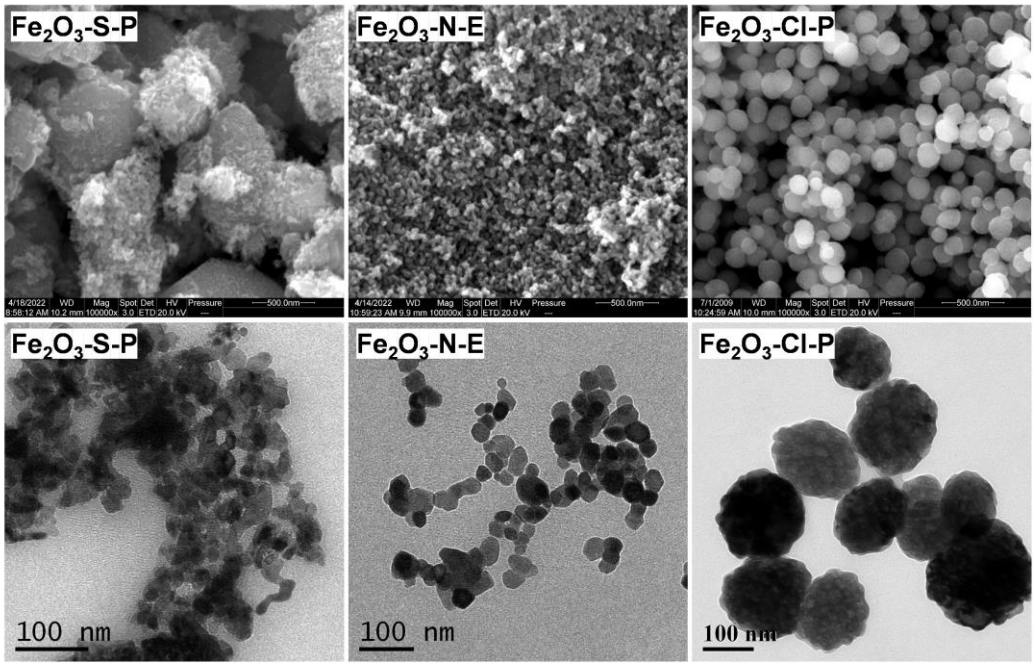

Figure 3. The SEM (**top**) and TEM (**bottom**) images of the as-prepared iron oxides.

2.1.3. Compositional and Structural Analyses of the Reduced Iron Oxides

The PXRD patterns of the Fe_2O_3 and the commercial Fe_3O_4–C after H_2 reduction at 350 °C were presented in Figure 4. The results can be grouped into two classes. Both Fe_2O_3–N–E and Fe_2O_3–S–P showed the predominant diffraction lines corresponding to the (110) facet of metallic iron (Fe^0 PDF # 06-0696) with the coexistence of relatively weak diffractions related to the (311) and (220) facets of Fe_3O_4 (PDF # 19-0629). On the contrary, all the typical diffraction patterns of Fe_3O_4 were found for Fe_2O_3–Cl–P and Fe_3O_4–C, but with quite different intensities. The above results suggested the different redox abilities of these samples, which will be studied in detail in the next sections. Furthermore, it means Fe_3O_4 was probably the predominant phase with the coexisted Fe^0 in Fe_2O_3–S–P and Fe_2O_3–N–E, while Fe_3O_4 was the main phase in Fe_2O_3–Cl–P and Fe_3O_4–C. Estimation of the crystallite sizes of Fe^0 based on the (110) facet revealed comparable values between Fe_2O_3–S–P and Fe_2O_3–N–E (57 vs. 52 nm), while the sizes of Fe_3O_4 based on the (311)

facet were determined to be 24, 53, 36, and 56 nm, respectively, for Fe_2O_3–S–P, Fe_2O_3–N–E, Fe_2O_3–Cl–P and Fe_3O_4–C.

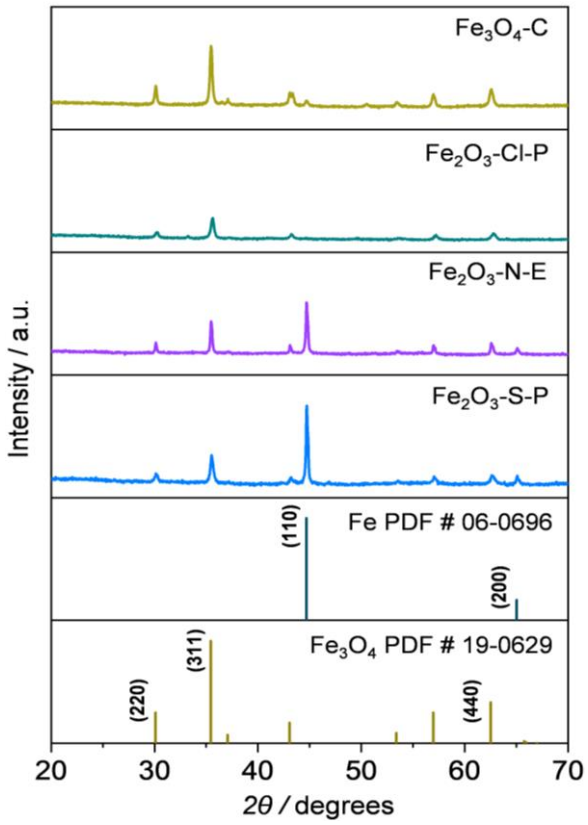

Figure 4. The PXRD patterns of the iron oxides after 350 °C reduction. Vertical lines are the reference standards.

The morphologies of the reduced samples were assessed by TEM (Figure 5). Fe_2O_3–S–P and Fe_2O_3–N–E showed irregular-shaped particles, while Fe_2O_3–Cl–P can still preserve the sphere-like morphology. As compared with un-reduced iron oxides, the particle sizes became much larger, hinting at the severe aggregation during the reduction treatments. Additionally, Fe_3O_4–C also showed big particles of irregular shapes. To further assess the structural differences, high-resolution TEM (HRTEM) analyses of the reduced samples were conducted(inset in Figure 5 and S1). Among all these materials, a clear core–shell structure was evidenced only in Fe_2O_3–S–P. Detailed analyses of this material revealed the continuous lattice fringes of Fe(111) with a distance of 2.0268 Å, and in the periphery, the lattice fringes of Fe_3O_4(111) with a distance of 2.5320 Å were found (Figure 6). These observations, therefore, ambiguously pointed to the formation of Fe^0 as the core covered with a thin shell of Fe_3O_4. As in the case of Fe_2O_3–S–P, the lattice fringes of both Fe(110) and Fe_3O_4(220) facets were observed in Fe_2O_3–N–E. These two facets were also in close proximity, suggesting the presence of Fe–Fe_3O_4 interfaces. In contrast, lattice fringe analyses of Fe_2O_3–Cl–P and Fe_3O_4–C only found the presence of the Fe_3O_4 phase. In general, the TEM observations were highly consistent with the PXRD results.

2.1.4. Redox Properties of the Iron Oxides

The redox properties of a catalytic material play an important role in the Fenton chemistry. Therefore, different techniques were applied to assess the redox properties of the as-derived iron oxides. The phase transitions of different iron compositions in flowing H_2 from room temperature to 700 °C were followed by in situ PXRD (Figure 7). Both Fe_2O_3–S–P and Fe_2O_3–N–E showed very similar phase transition patterns. Namely, the Fe_3O_4 phase in these two samples vanished at much lower temperatures as compared

with Fe_2O_3–Cl–P (658–673 vs. 746 °C). Meanwhile, the appearance of Fe^0 diffractions emerged at significantly lower temperatures (493–523 vs. 627 °C). Differing from the three as-prepared Fe_2O_3 materials, which showed the reduction to different degrees, the in situ PXRD patterns of Fe_3O_4–C indicated that this material was extremely difficult to reduce. The Fe_3O_4 phase predominated with only very weak diffractions related to Fe^0. Overall, these results suggested the very different reduction propensities of the materials with the order of Fe_2O_3–S–P ~ Fe_2O_3–N–E > Fe_2O_3–Cl–P >> Fe_3O_4–C.

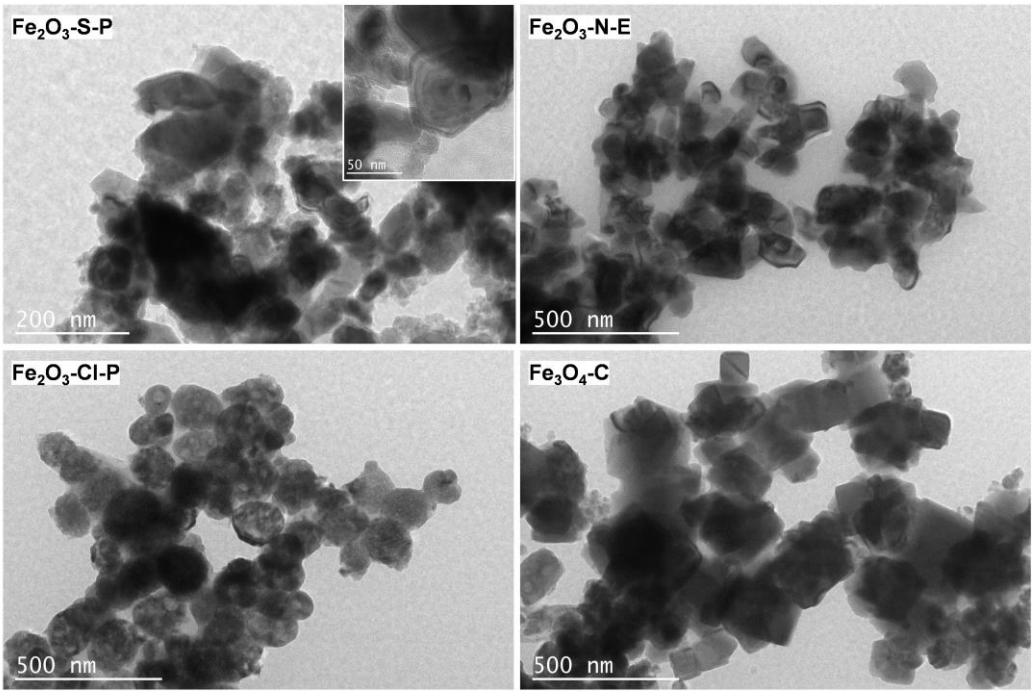

Figure 5. The TEM images of the iron oxides after 350 °C reduction. The inset in top-left shows the core–shell structures in Fe_2O_3–S–P.

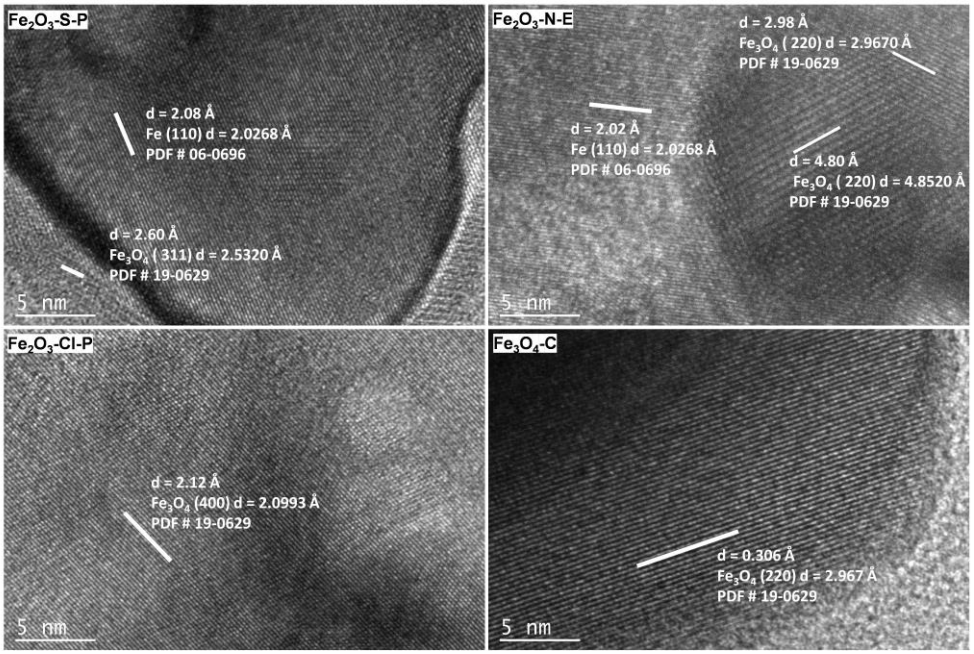

Figure 6. The HRTEM images of the iron oxides after 350 °C reduction.

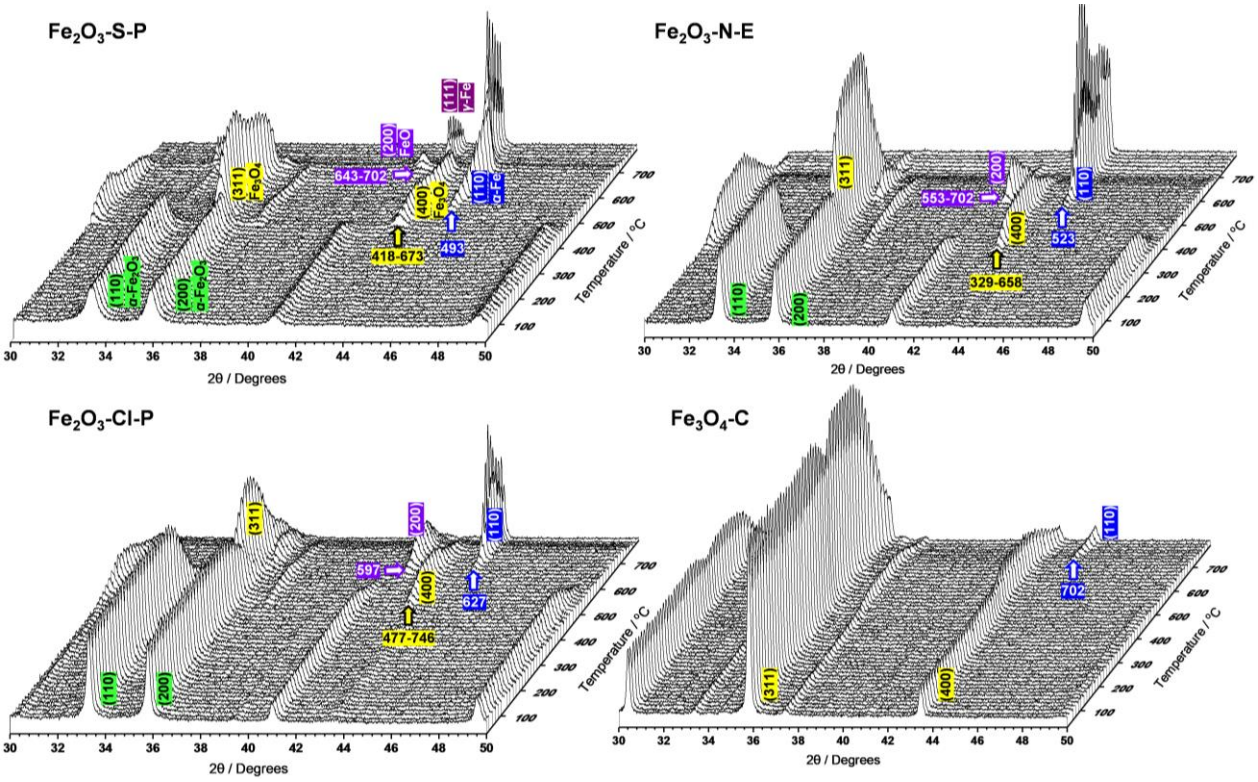

Figure 7. The in situ PXRD patterns of the iron oxides in flowing H_2.

2.1.5. Surface Iron Species and Oxygen Vacancy

The different surface iron and oxygen species of the reduced iron oxides were studied by X-ray photoelectron spectroscopy (XPS, Figure 8), as they were suggested to have important influences on the redox and Fenton chemistry. The Fe 2p spectra of all the samples showed a doublet at 736–706 eV with a satellite around 718 eV. The spectra were analyzed by peak fitting with Fe^{2+} and Fe^{3+} species with known peak positions from the literature results. It was determined that the shares of Fe^{2+} were comparable for Fe_2O_3–S–P, Fe_2O_3–Cl–P, and Fe_3O_4–C (44–46%) and were much higher than that of Fe_2O_3–N–E (35%). The O 1*s* of these reduced samples were also analyzed by fitting the spectra. It was revealed that Fe_2O_3–S–P, Fe_2O_3–Cl–P, and Fe_3O_4–C possessed similar shares of oxygen vacancy (O_v, 30–36%), while it was the lowest for Fe_2O_3–N–E (14%).

2.2. Performance in MO Decomposition

The catalytic performance of the derived iron oxides was evaluated in the decomposition of methyl orange that was chosen as a model reaction to assess the Fenton chemistry. All the materials were reduced in H_2 at 350 °C and stored in air at room temperature for more than 24 h prior to the tests. At first, the activity was evaluated at a lower MO concentration of 100 μg/mL (Figure 9a). The conversion steadily increased for Fe_2O_3–Cl–P and Fe_3O_4–C. While full conversion was already achieved at 60 min for Fe_2O_3–C, the conversion only slowly increased and stayed at about 22% at 120 min for Fe_2O_3–Cl–P. In stark contrast, full conversion was readily achieved upon the addition of H_2O_2 for both Fe_2O_3–S–P and Fe_2O_3–N–E. To further discriminate the activity difference, the decomposition activity was further evaluated at a higher MO concentration of 500 μg/mL (Figure 9b). Under such conditions, full conversion was still readily reached at 30 min for Fe_2O_3–S–P. In contrast, the conversions at 120 min were only 80% and 35%, respectively, for Fe_2O_3–N–E and Fe_3O_4–C. To quantitatively compare the Fenton activity of the four samples, the initial reaction rates were calculated by considering the linear parts of the conversion-time profiles (Figure 9c). Fe_2O_3–S–P exhibited the highest rate of 370 $mg_{MO}\ g_{cat}^{-1}\ min^{-1}$, which is 2 times higher than that of Fe_2O_3–N–E and significantly outperforms Fe_2O_3–Cl–P and

Fe_3O_4–C by 1–2 orders of magnitude. In order to confirm that the reaction proceeded in a heterogeneous manner, we conducted another test by replacing the iron oxides with trace $Fe(NO_3)_3$ so as to mimic the leaching of iron species into the solution. It turned out that the MO decomposition occurred roughly slowly in the first 30 min, and a low conversion of ca. 26% was reached for 120 min (Figure S2). The extremely slow kinetics, as compared with the highly active Fe_2O_3–S–P and Fe_2O_3–N–E, thus suggested the heterogeneous nature of the decomposition reaction on the latter. The cycling performance of Fe_2O_3–S–P was attempted. To fully recover the solid catalyst after use, the catalyst amount and the volume of wastewater were scaled up by four folds. Under such conditions, similar kinetics were achieved in the two consecutive cycles, although full removal of MO cannot be reached in 120 min (Figure S3). The relatively lower activity in the scale-up tests might be caused by the mass transfer effect. In addition, the dissolved iron in the solution after the first cycle was determined to be ca. 48 ppm by inductively coupled plasma optical emission spectroscopy (ICP-OES).

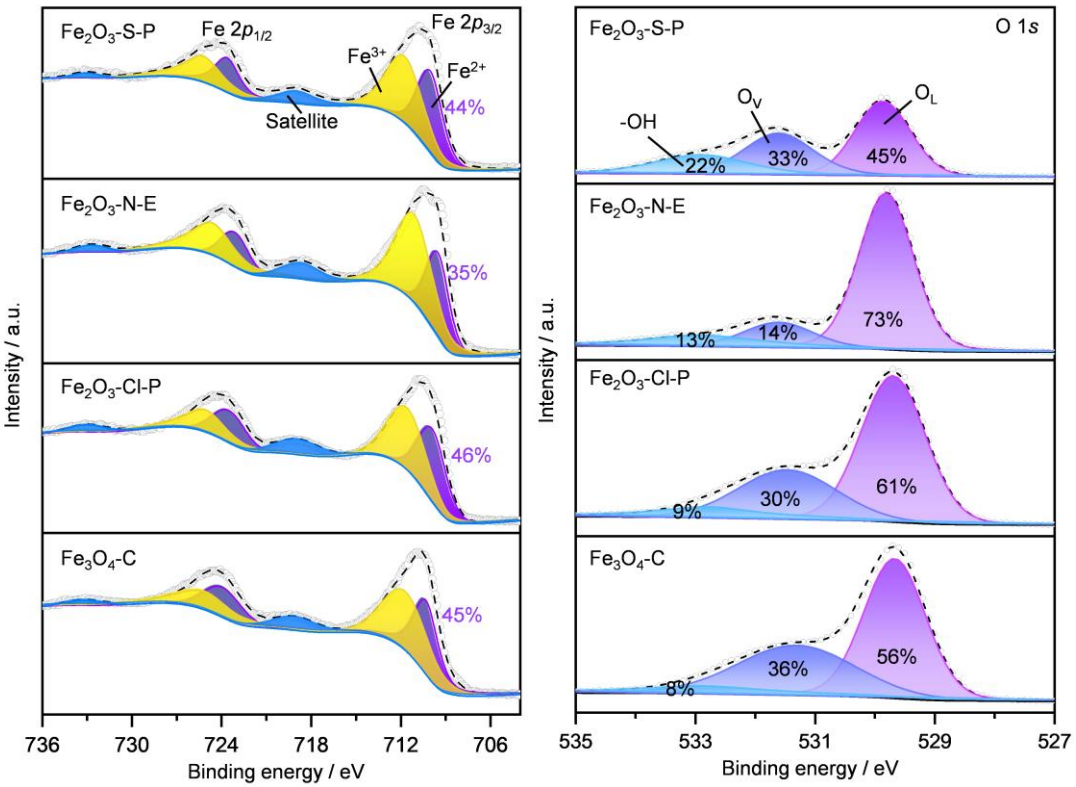

Figure 8. The Fe 2*p* and O 1*s* *XPS* profiles of the iron oxides after 350 °C reduction. O_v—oxygen vacancy; O_L—lattice oxygen.

2.3. Origins of the Divergent Catalytic Performance

2.3.1. Structure–Performance Relationships

The Fenton activity of iron-based materials can be influenced by many factors, which makes it difficult to discriminate the key activity descriptors. Among the suspected properties, the Fe^{2+} species, the oxygen vacancy, and redox properties might play important roles in influencing the activity. Therefore, tentative correlations were made between the initial reaction rates with the shares of Fe^{2+} and O_v derived from the XPS fitting and the T_{Fe} (the temperature corresponding to the appearance of the Fe^0 phase from in situ PXRD, Figure 10). We noted that T_{Fe} was adopted to roughly reflect the redox properties of the iron oxides. The results demonstrated that there was no clear dependence of the initial activity on either the shares of Fe^{2+} or O_v, whereas increasing activity as a function of

decreasing T_{Fe} was evidenced. Therefore, it seems that the redox propensity might be a reasonable activity descriptor in the Fenton chemistry.

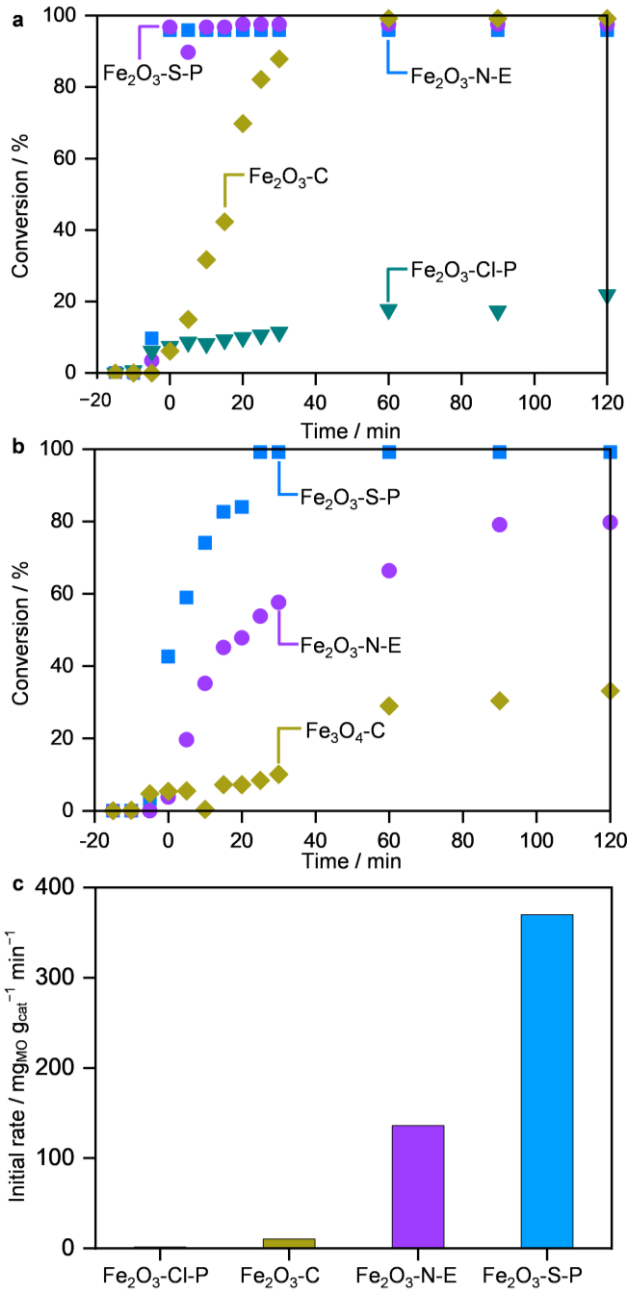

Figure 9. (**a**,**b**) The MO decomposition activity as a function of time on different iron oxides. (**c**) Comparison of the initial activity of different iron oxides. Reaction conditions: w_{cat} = 5 mg (350 °C reduced); pH = 3, V = 100 mL, C_{H2O2} = 20 mM; (**a**) C_{MO} = 100 μg/mL, (**b**) C_{MO} = 500 μg/mL. The first three data points before the addition of H_2O_2 correspond to the freshly prepared solution, the solutions after the adjustment in pH, and after 30 min stirring, respectively.

2.3.2. Importance of the Fe@Fe_3O_4 Interfaces

The detailed characterization of the iron oxides revealed that both Fe^0 and Fe_3O_4 were formed on Fe_2O_3–S–P and Fe_2O_3–N–E, while only Fe_3O_4 existed on Fe_2O_3–Cl–P and Fe_3O_4–C. Thus, it is reasonable to speculate that the presence of Fe^0 was crucial to the high Fenton activity. To further discriminate the MO decomposition performance of the different compositions of iron species, Fe_2O_3–S–P reduced in H_2 at varying temperatures from

300 to 450 °C was conducted. The PXRD results confirmed that Fe_2O_3 was the major phase after 300 °C reduction (Figure 11). After reduction at 350 °C, Fe^0 was the major phase with the coexistence of Fe_3O_4. After further increasing the temperature to 450 °C, Fe^0 was the only phase.

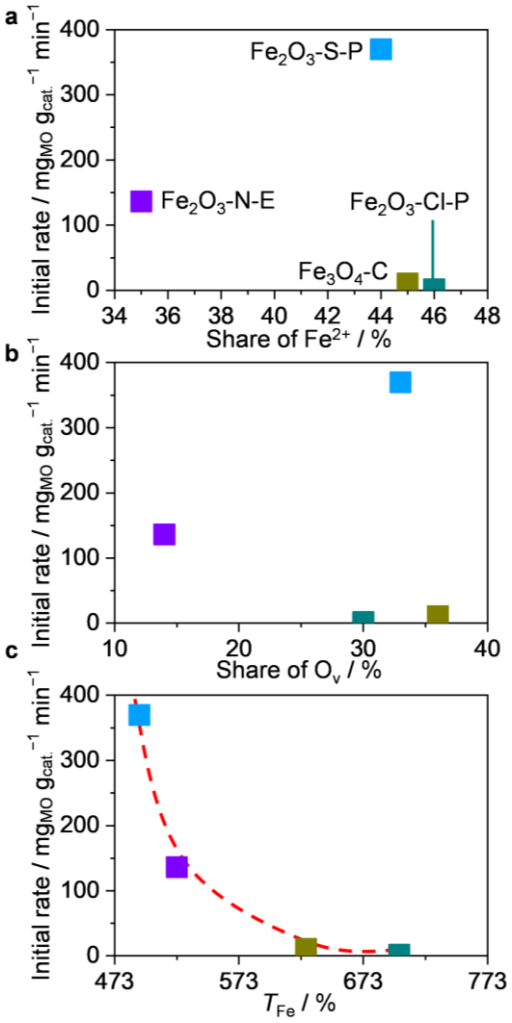

Figure 10. The initial reaction rates of different iron oxides as a function of (**a**) surface Fe^{2+} ratio, (**b**) oxygen vacancy, and (**c**) T_{Fe} (the temperature corresponding to the appearance of Fe^0 phase from in situ PXRD). T_{Fe} can be viewed as an indicator of the redox properties of the respective catalysts.

Having derived different compositions of the iron-based materials from Fe_2O_3–S–P, their activity in MO decomposition was evaluated (Figure 12). The results showed that the samples reduced at 350 and 450 °C displayed basically the same activity, whereas no appreciable conversion can be observed for the unreduced sample and after 300 °C reduction. Combined with the activity evaluation, it can be concluded that Fe^0 or Fe^0/Fe_3O_4 were responsible for the catalytic activity, but both Fe_3O_4 and Fe_2O_3, when used alone, were completely inactive in Fenton chemistry.

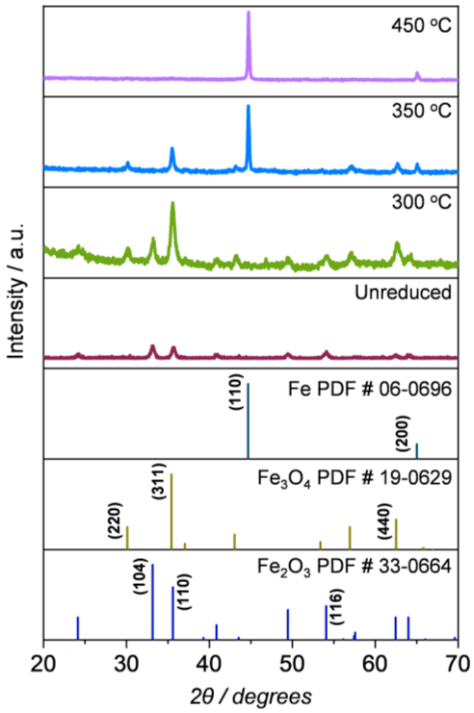

Figure 11. The PXRD patterns of Fe_2O_3–S–P after reduction in H2 at 300–450 °C. Vertical lines are the reference standards.

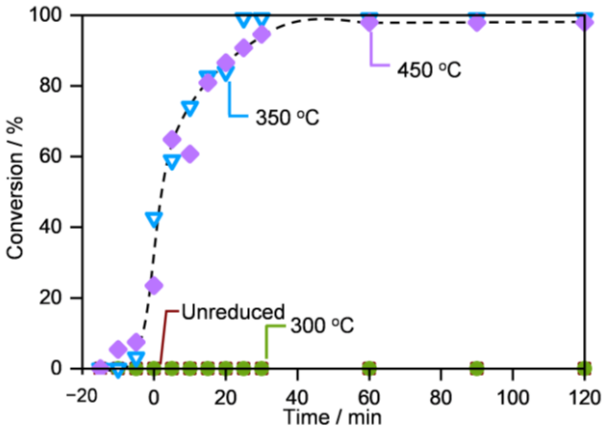

Figure 12. The MO decomposition activity as a function of time on Fe_2O_3–S–P subject to H_2 reduction at different temperatures. Reaction conditions: w_{cat} = 5 mg, pH = 3, V = 100 mL, C_{H2O2} = 20 mM, C_{MO} = 500 μg/mL. The first three data points before the addition of H_2O_2 correspond to the freshly prepared solution, the solutions after the adjustment in pH, and after 30 min stirring, respectively.

Although the iron oxide in Fe_2O_3–S–P was completely converted into Fe^0 after 450 °C reduction based on PXRD, the exposure to air should easily lead to the formation of a thin oxide layer. It means for this sample, both Fe^0 and Fe_3O_4 might co-exist, like in the case of the sample reduced at 350 °C. To prove the speculation, XPS with depth profile analysis was performed on Fe_2O_3–S–P after 450 °C and exposure to air (Figure 13). The fitting of the Fe 2*p* XPS spectra evidently revealed the exclusive presence of both Fe^{3+} and Fe^{2+} species at the outer surfaces, while the contribution of Fe^0 emerged up to a depth of 11.4 nm, and the share became larger, subject to further sputtering. The results thus confirmed the formation of an iron oxide layer of ca. 11–17 nm thickness owing to the auto-oxidation of metallic iron. In addition, the previous TEM and PXRD results of Fe_2O_3–S–P after 350 °C reduction also indicated the presence of the Fe@Fe_3O_4 core–shell structure and a thickness of Fe_3O_4 layer of <24 nm. Therefore, the similar activity of Fe_2O_3–S–P subject to

350–400 °C reduction can be attributed to the presence of similar Fe@Fe_3O_4 core–shell structures. On the other hand, Fe_2O_3–N–E with both Fe^0 and Fe_3O_4 as the major phases without the apparent core–shell structures exhibited relatively lower activity as compared to Fe_2O_3–S–P. Albeit an interface between both phases was confirmed by HRTEM, no core–shell structures can be observed, plus the Fe_3O_4 particle sizes (ca. 54 nm) were much larger as compared with the layer thickness in Fe_2O_3–S–P. These factors might lead to a reduced number of interface structures and, thus, lower activity.

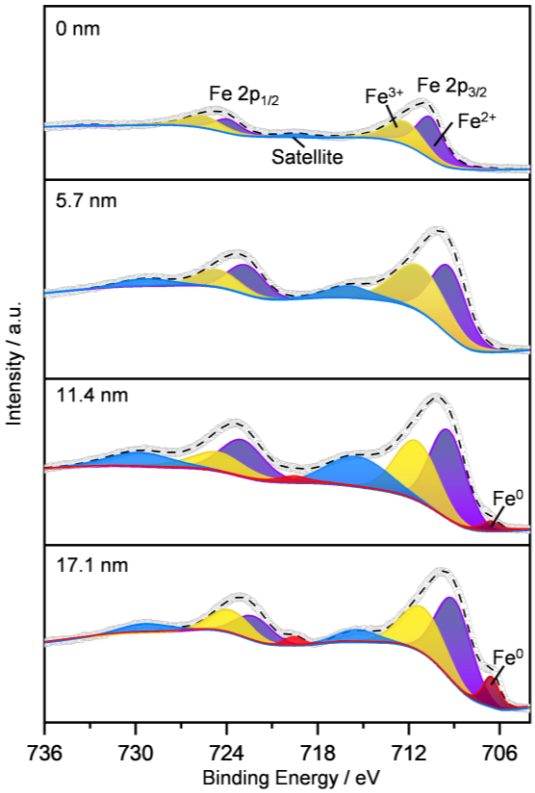

Figure 13. The Fe 2*p XPS* depth profiles of Fe_2O_3–S–P after 450 °C reduction. All the samples were stored in air at room temperature for more than 24 h.

2.3.3. Discussions on the Origin of Superior Activity

The formation of radicals such as OH* and HO_2* was generally acknowledged to be responsible for the MO decomposition in the Fenton chemistry. Indeed, the reaction was immediately jeopardized upon the addition of a radical trapper such as dimethyl sulfoxide (Figure S4), demonstrating the radical-induced nature of this reaction. Both Fe_2O_3–Cl–P and Fe_3O_4–C showed comparable rich surface Fe^{2+} species and O_v but without the presence of ZVI. In contrast, Fe_2O_3–N–E containing ZVI but with a lower number of O_v also displayed inferior activity. These results hinted that the superior Fenton activity of Fe_2O_3–S–P with the Fe@Fe_3O_4 core–shell structures might be attributed to the abundance of both Fe^0 and O_v. The rate-limiting step in the heterogeneous Fenton reaction is viewed as the formation of Fe^{2+} species that are responsible for generating highly active OH* through Equation (1). Previous studies have proposed that Fe^{2+} species might be produced by the oxidation of ZVI by H_2O_2 or molecular oxygen in acidic conditions [40,41]. In addition, the studies on the Fe@Fe_2O_3 systems also suggested the excellent reducing properties of metallic iron to achieve a high Fe^{2+}/Fe^{3+} redox cycling rate, wherein ZVI can directly inject two electrons to activate molecular oxygen [42,43]. On the other hand, the rich number of O_v has been demonstrated to be beneficial to the generation of OH* [44–47]. Li et al. [46] confirmed that H_2O_2 adsorbed on the electron-rich location readily underwent dissociation induced by O_v (Equation (2)). Chen et al. [44] reported the accelerated electron transfer

process and threefold yield of OH* for the O_v-rich micro ZVI interface. The synergistic cooperation catalysis between ZVI and iron oxides was proposed in Equation (3). Following this equation, the surface-bonded Fe^{2+} species were generated between the iron oxides and O_v. The surface-bonded Fe^{2+} species were suggested to be more reactive than ferrous ions in activating H_2O_2, thus avoiding the rate-limiting step in the classic Fenton reaction.

$$H_2O_2 + Fe^{2+} \rightarrow Fe^{3+} + OH^* + OH^- \quad (1)$$

$$H_2O_2 + O_v \rightarrow OH^* + OH^- \quad (2)$$

$$Fe_xO_y + O_v \rightarrow e^- + Fe^{2+}{}_{(sur)} \quad (3)$$

3. Materials and Methods

3.1. Synthesis of the Iron Oxides

All the reagents were obtained from commercial suppliers and used without further purification. $Fe(NH_4)_2(SO_4)_2{\cdot}6H_2O$(99.5%), $Fe(NO_3)_3{\cdot}9H_2O$, and $FeCl_3{\cdot}6H_2O$ were purchased from Aladdin. Polyethylene glycol 400 (PEG-400), ethylene glycol (EG, ≥99.5%), and sodium carbonate (Na_2CO_3, ≥99.8%) were purchased from Sinopharm. Ammonium hydroxide solution ($NH_3{\cdot}H_2O$,25–28%) and Fe_3O_4–C (99.5%) were purchased from Macklin.

The other three iron oxides were prepared by a precipitation method. A solution containing $Fe(NH_4)_2(SO_4)_2{\cdot}6H_2O$ (0.02 mol/L) and polyethylene glycol 400 (200 mL) was gradually heated to 120 °C under mechanical stirring and maintained at 120 °C for 1 h. Then a Na_2CO_3 aqueous solution (200 mL, 0.2 mol/L) was added gradually dropwise through a syringe pump at a rate of 5.5 mL/min. The mixture was aged at 120 °C for 1 h. The precipitate was washed with water and ethanol, dried at 120 °C for 12 h, and calcined at 500 °C for 5 h. The solids obtained, which were denoted as Fe_2O_3–S–P, Fe_2O_3–N–E, and Fe_2O_3–Cl–P, were obtained following similar precipitation methods by using $Fe(NO_3)_3{\cdot}9H_2O$ and $FeCl_3{\cdot}6H_2O$ as the precursors, EG and PEG-400 as the solvents, and sodium carbonate concentrations of 0.02 and 0.2 M, respectively.

3.2. Material Characterizations

The composition and crystalline structures of the catalysts were characterized by powder X-ray diffraction (PXRD) with an x'Pert3 Panalytical X-ray diffractometer (PANalytical, Almelo, The Netherlands) using Cu K_α radiation (λ = 0.154178 nm). The tube voltage and current were 40 kV and 40 mA, respectively. In situ PXRD patterns were recorded with Rigaku SmartLab-9 kW D/teX Ultra250 diffractometer using a Cu K_α radiation source operated at 40 kV and 200 mA. The powder samples were spread into a high-temperature chamber, and the diffraction patterns were recorded at 2θ of 30–90° with a scanning rate of 10° min^{-1} at room temperature. Then, the sample was heated to 823 K successively at a rate of 10 °C min^{-1} under 10% H_2/He flow of 30 mL min^{-1}.

Scanning electron microscopy (SEM) was conducted on a Quanta 200F instrument operating at 10 kV and 50 pA. The powder sample was dispersed in dry form onto fresh carbon paint deposited on an aluminum holder.

Transmission electron microscopy (TEM) images were taken on an FEI Tecnai G2F 20 microscopy operating at 120 kV. The specimen was prepared by ultrasonically dispersing the powder sample in ethanol, depositing droplets of the suspensions onto carbon-coated copper or gold grids, and drying in air.

X-ray photoelectron spectroscopy (XPS) analysis of the materials was performed on a Thermo ESCALAB 250Xi spectrometer using a 15 kV Al K_α X-ray source as a radiation source. The binding energy was calibrated using the C 1*s* peak (284.6 eV) as the reference. For the depth profile analysis, the samples were sputtered with Ar ions.

The iron content in the solution after the catalytic test was measured by inductively coupled plasma optical emission spectroscopy (ICP-OES) on a Perkin-Elmer Optima 7300DV.

3.3. Activity Evaluation of the Iron-Based Materials in Decomposition of Methyl Orange

The activity evaluation of the developed iron-based materials in the decomposition of methyl orange (MO) was performed in a 250 mL three-necked round flask equipped with a magnetic stirrer and a temperature thermometer. The temperature was controlled by a pre-heated water bath. For a typical reaction, 100 mL of aqueous MO solutions of 100 or 500 μg/mL were charged into the flask reactor. The pH of the solution was then adjusted to 3.0 by diluted HCl solution. After that, a certain amount of the solid catalysts was added, and the suspension was stirred for 30 min to reach the adsorption–desorption equilibrium. Finally, the reaction was initiated upon the addition of a diluted H_2O_2 solution, and the concentration of MO was continuously monitored by taking a small portion of the liquid samples for analysis on a UV–Vis spectrometer (TU-1810, Beijing Puxi General Motors Instrument Co.) at λ_{max} = 464 nm (see Figure S5 for more details).

4. Conclusions

We have developed iron oxides of four different model systems through the conventional precipitation method by combining them with subsequent H_2 reduction treatment. These materials possess very different compositions and structural features, including the Fe@Fe_3O_4 core–shell structures with rich oxygen vacancy (Fe_2O_3–S–P), the mixtures of Fe^0 and Fe_3O_4 particles with interface structures but low oxygen vacancy (Fe_2O_3–N–E), and Fe_3O_4-dominated nanoparticles of different sizes and rich in oxygen vacancy (Fe_2O_3–Cl–P and Fe_3O_4–C). These materials, when used as Fenton catalysts in the methyl orange decomposition, displayed significantly different activity with the order of Fe_2O_3–S–P > Fe_2O_3–N–E > Fe_3O_4–C > Fe_2O_3–Cl–P. The passivating layer of metallic iron of up to ca. 24 nm can lead to similar Fe@Fe_3O_4 core–shell structures with excellent activity. This study further demonstrated that the numbers of Fe^{2+} or oxygen vacancy alone might not be the only activity descriptors for the iron-based materials, while the formation of metallic iron coupled with the rich oxygen vacancy can significantly boost the Fenton activity, thus highlighting the necessity of more in-depth analyses of the role of the hybrid Fe@Fe_xO_y.

Supplementary Materials: The following supporting information can be downloaded at https://www.mdpi.com/article/10.3390/catal13071057/s1, Figure S1: The additional TEM images of the iron oxides after 350 °C reduction. Figure S2: The MO decomposition activity as a function of time in the presence of an Fe^{3+} solution. Reaction conditions: C_{MO} = 100 μg/mL, pH = 3, 2.6 mg $Fe(NO_3)_3 \bullet 9H_2O$, and C_{H2O2}= 20 mM. Figure S3: The kinetic profiles of MO decomposition on Fe_2O_3-S-P in two consecutive runs. Reaction conditions: w_{cat} = 20 mg; pH = 3, V = 400 mL, C_{H2O2}= 80 mM, C_{MO} = 500 μg/mL. The catalyst after the use was recovered by centrifugation. Figure S4: The MO decomposition activity as a function of time on Fe_2O_3-N-E. DMSO was added at 5 min, and the conversion did not increase hereafter, thus demonstrating the radical induction nature of the reaction. Figure S5: (a) The absorbance of MO solutions of different concentrations as a function of the wavelength, and (b) the linear relationship between the MO concentration and the absorbance intensity at 464 nm.

Author Contributions: Conceptualization, X.M. and W.K.; investigation, R.Z., J.Q. and R.T.; XRD and XPS, Y.L.; TEM, R.L.; writing—review and editing, X.M., P.F. and W.K. All authors have read and agreed to the published version of the manuscript.

Funding: This research received no external funding.

Data Availability Statement: All data are available from the authors upon request.

Acknowledgments: The authors would like to thank Deiyou Chen from Shiyanjia Lab (www.shiyanjia.com, accessed on 1 May 2023) for TEM measurements.

Conflicts of Interest: The authors declare no conflict of interest.

References

1. Tran, N.H.; Reinhard, M.; Gin, K.Y.-H. Occurrence and fate of emerging contaminants in municipal wastewater treatment plants from different geographical regions-a review. *Water Res.* **2018**, *133*, 182–207. [CrossRef]
2. Hodges, B.C.; Cates, E.L.; Kim, J.H. Challenges and prospects of advanced oxidation water treatment processes using catalytic nanomaterials. *Nat. Nanotechnol.* **2018**, *13*, 642–650. [CrossRef]
3. Boczkaj, G.; Fernandes, A. Wastewater treatment by means of advanced oxidation processes at basic pH conditions: A review. *Chem. Eng. J.* **2017**, *320*, 608–633. [CrossRef]
4. Altalhi, T.A.; Ibrahim, M.M.; Mersal, G.A.M.; Mahmoud, M.H.H.; Kumeria, T.; El-Desouky, M.G.; El-Bindary, A.A.; El-Bindary, M.A. Adsorption of doxorubicin hydrochloride onto thermally treated green adsorbent: Equilibrium, kinetic and thermodynamic studies. *J. Mol. Struct.* **2022**, *1263*, 133160. [CrossRef]
5. Bokare, A.D.; Choi, W. Review of iron-free Fenton-like systems for activating H2O2 in advanced oxidation processes. *J. Hazard. Mater.* **2014**, *275*, 121–135. [CrossRef]
6. Zhu, Y.; Zhu, R.; Xi, Y.; Zhu, J.; Zhu, G.; He, H. Strategies for enhancing the heterogeneous Fenton catalytic reactivity: A review. *Appl. Catal. B* **2019**, *255*, 117739. [CrossRef]
7. He, J.; Yang, X.; Men, B.; Wang, D. Interfacial mechanisms of heterogeneous Fenton reactions catalyzed by iron-based materials: A review. *J. Environ. Sci.* **2016**, *39*, 97–109. [CrossRef]
8. Rahim Pouran, S.; Abdul Raman, A.A.; Wan Daud, W.M.A. Review on the application of modified iron oxides as heterogeneous catalysts in Fenton reactions. *J. Clean. Prod.* **2014**, *64*, 24–35. [CrossRef]
9. Zepp, R.G.; Faust, B.C.; Hoigne, J. Hydroxyl radical formation in aqueous reactions (pH 3–8) of iron (II) with hydrogen peroxide: The photo-Fenton reaction. *Environ. Sci. Technol.* **1992**, *26*, 313–319. [CrossRef]
10. Oller, I.; Malato, S.; Sánchez-Pérez, J.; Gernjak, W.; Maldonado, M.; Pérez-Estrada, L.; Pulgarín, C. A combined solar photocatalytic-biological field system for the mineralization of an industrial pollutant at pilot scale. *Catal. Today* **2007**, *122*, 150–159. [CrossRef]
11. Malato, S.; Fernández-Ibáñez, P.; Maldonado, M.I.; Blanco, J.; Gernjak, W. Decontamination and disinfection of water by solar photocatalysis: Recent overview and trends. *Catal. Today* **2009**, *147*, 1–59. [CrossRef]
12. Brillas, E.; Sirés, I.; Oturan, M.A. Electro-Fenton process and related electrochemical technologies based on Fenton's reaction chemistry. *Chem. Rev.* **2009**, *109*, 6570–6631. [CrossRef] [PubMed]
13. Adewuyi, Y.G. Sonochemistry in environmental remediation. 1. Combinative and hybrid sonophotochemical oxidation processes for the treatment of pollutants in water. *Environ. Sci. Technol.* **2005**, *39*, 3409–3420. [CrossRef]
14. Cai, W.; Chen, F.; Shen, X.; Chen, L.; Zhang, J. Enhanced catalytic degradation of AO7 in the CeO_2–H_2O_2 system with Fe^{3+} doping. *Appl. Catal. B* **2010**, *101*, 160–168. [CrossRef]
15. Bokare, A.D.; Choi, W. Advanced oxidation process based on the Cr (III)/Cr (VI) redox cycle. *Environ. Sci. Technol.* **2011**, *45*, 9332–9338. [CrossRef]
16. Gabriel, J.; Baldrian, P.; Verma, P.; Cajthaml, T.; Merhautová, V.; Eichlerová, I.; Stoytchev, I.; Trnka, T.; Stopka, P.; Nerud, F. Degradation of BTEX and PAHs by Co (II) and Cu (II)-based radical-generating systems. *Appl. Catal. B* **2004**, *51*, 159–164. [CrossRef]
17. Gabriel, J.; Shah, V.; Nesměrák, K.; Baldrian, P.; Nerud, F. Degradation of polycyclic aromatic hydrocarbons by the copper (II)-hydrogen peroxide system. *Folia Microbiol.* **2000**, *45*, 573–575. [CrossRef]
18. Han, Y.-F.; Chen, F.; Zhong, Z.; Ramesh, K.; Chen, L.; Jian, D.; Ling, W.W. Complete oxidation of low concentration ethanol in aqueous solution with H_2O_2 on nanosized Mn_3O_4/SBA-15 catalyst. *Chem. Eng. J.* **2007**, *134*, 276–281. [CrossRef]
19. Hu, Z.; Leung, C.-F.; Tsang, Y.-K.; Du, H.; Liang, H.; Qiu, Y.; Lau, T.-C. A recyclable polymer-supported ruthenium catalyst for the oxidative degradation of bisphenol A in water using hydrogen peroxide. *New J. Chem.* **2011**, *35*, 149–155. [CrossRef]
20. Mizuno, N.; Yamaguchi, K.; Kamata, K. Epoxidation of olefins with hydrogen peroxide catalyzed by polyoxometalates. *Coord. Chem. Rev.* **2005**, *249*, 1944–1956. [CrossRef]
21. Huang, J.; Jones, A.; Waite, T.D.; Chen, Y.; Huang, X.; Rosso, K.M.; Kappler, A.; Mansor, M.; Tratnyek, P.G.; Zhang, H. Fe(II) Redox chemistry in the environment. *Chem. Rev.* **2021**, *121*, 8161–8233. [CrossRef]
22. Danielsen, K.M.; Hayes, K.F. pH Dependence of carbon tetrachloride reductive dechlorination by magnetite. *Environ. Sci. Technol.* **2004**, *38*, 4745–4752. [CrossRef]
23. Gorski, C.A.; Nurmi, J.T.; Tratnyek, P.G.; Hofstetter, T.B.; Scherer, M.M. Redox behavior of magnetite: Implications for contaminant reduction. *Environ. Sci. Technol.* **2010**, *44*, 55–60. [CrossRef]
24. Zhong, Y.; Yu, L.; Chen, Z.F.; He, H.; Ye, F.; Cheng, G.; Zhang, Q. Microwave-assisted synthesis of Fe_3O_4 nanocrystals with predominantly exposed facets and their heterogeneous UVA/Fenton catalytic activity. *ACS Appl. Mater. Interface.* **2017**, *9*, 29203–29212. [CrossRef]
25. Jaramillo-Páez, C.; Navío, J.A.; Hidalgo, M.; Bouziani, A.; El Azzouzi, M. Mixed α-Fe_2O_3/Bi_2WO_6 oxides for photoassisted hetero-Fenton degradation of Methyl Orange and Phenol. *J. Photochem. Photobiol. A* **2017**, *332*, 521–533. [CrossRef]
26. Ma, Y.; Wang, B.; Wang, Q.; Xing, S. Facile synthesis of α-FeOOH/γ-Fe_2O_3 by a pH gradient method and the role of γ-Fe_2O_3 in H_2O_2 activation under visible light irradiation. *Chem. Eng. J.* **2018**, *354*, 75–84. [CrossRef]
27. Krumina, L.; Lyngsie, G.; Tunlid, A.; Persson, P. Oxidation of a dimethoxyhydroquinone by ferrihydrite and goethite nanoparticles: Iron reduction versus surface catalysis. *Environ. Sci. Technol.* **2017**, *51*, 9053–9061. [CrossRef]

28. Su, S.; Liu, Y.; Liu, X.; Jin, W.; Zhao, Y. Transformation pathway and degradation mechanism of methylene blue through β-FeOOH@ GO catalyzed photo-Fenton-like system. *Chemosphere* **2019**, *218*, 83–92. [CrossRef]
29. He, D.; Chen, Y.; Situ, Y.; Zhong, L.; Huang, H. Synthesis of ternary g-C_3N_4/Ag/γ-FeOOH photocatalyst: An integrated heterogeneous Fenton-like system for effectively degradation of azo dye methyl orange under visible light. *Appl. Surf. Sci.* **2017**, *425*, 862–872. [CrossRef]
30. Chen, Z.X.; Jin, X.Y.; Chen, Z.; Megharaj, M.; Naidu, R. Removal of methyl orange from aqueous solution using bentonite-supported nanoscale zero-valent iron. *J. Colloid Interface Sci.* **2011**, *363*, 601–607. [CrossRef]
31. Xie, S.; Huang, P.; Kruzic, J.J.; Zeng, X.; Qian, H. A highly efficient degradation mechanism of methyl orange using Fe-based metallic glass powders. *Sci. Rep.* **2016**, *6*, 21947. [CrossRef]
32. Yuan, N.; Zhang, G.; Guo, S.; Wan, Z. Enhanced ultrasound-assisted degradation of methyl orange and metronidazole by rectorite-supported nanoscale zero-valent iron. *Ultrason. Sonochem.* **2016**, *28*, 62–68. [CrossRef]
33. Zhu, L.; Ai, Z.; Ho, W.; Zhang, L. Core–shell Fe–Fe_2O_3 nanostructures as effective persulfate activator for degradation of methyl orange. *Sep. Purif. Technol.* **2013**, *108*, 159–165. [CrossRef]
34. Huang, Q.; Cao, M.; Ai, Z.; Zhang, L. Reactive oxygen species dependent degradation pathway of 4-chlorophenol with Fe@Fe_2O_3 core–shell nanowires. *Appl. Catal. B* **2015**, *162*, 319–326. [CrossRef]
35. Shen, W.; Lin, F.; Jiang, X.; Li, H.; Ai, Z.; Zhang, L. Efficient removal of bromate with core-shell Fe@Fe_2O_3 nanowires. *Chem. Eng. J.* **2017**, *308*, 880–888. [CrossRef]
36. Shi, J.; Ai, Z.; Zhang, L. Fe@Fe_2O_3 core-shell nanowires enhanced Fenton oxidation by accelerating the Fe (III)/Fe(II) cycles. *Wat. Res.* **2014**, *59*, 145–153. [CrossRef] [PubMed]
37. Liu, W.; Ai, Z.; Cao, M.; Zhang, L. Ferrous ions promoted aerobic simazine degradation with Fe@Fe_2O_3 core–shell nanowires. *Appl. Catal. B* **2014**, *150*, 1–11. [CrossRef]
38. Ai, Z.; Gao, Z.; Zhang, L.; He, W.; Yin, J.J. Core–shell structure dependent reactivity of Fe@Fe_2O_3 nanowires on aerobic degradation of 4-chlorophenol. *Environ. Sci. Technol.* **2013**, *47*, 5344–5352. [CrossRef]
39. Daliran, S.; Khajeh, M.; Oveisi, A.R. A porous Fe-based porphyrinic metal–organic framework for highly effective removal of organic azo-dye. *Appl. Organomet. Chem.* **2022**, *36*, e6830. [CrossRef]
40. Costa, R.C.; Moura, F.C.; Ardisson, J.; Fabris, J.; Lago, R. Highly active heterogeneous Fenton-like systems based on Fe^0/Fe_3O_4 composites prepared by controlled reduction of iron oxides. *Appl. Catal. B* **2008**, *83*, 131–139. [CrossRef]
41. Leupin, O.X.; Hug, S.J. Oxidation and removal of arsenic (III) from aerated groundwater by filtration through sand and zero-valent iron. *Water Res.* **2005**, *39*, 1729–1740. [CrossRef]
42. Wu, H.; Ai, Z.; Zhang, L. Anoxic and oxic removal of humic acids with Fe@Fe_2O_3 core–shell nanowires: A comparative study. *Water Res.* **2014**, *52*, 92–100. [CrossRef] [PubMed]
43. Wang, L.; Cao, M.; Ai, Z.; Zhang, L. Dramatically enhanced aerobic atrazine degradation with Fe@Fe_2O_3 core–shell nanowires by tetrapolyphosphate. *Environ. Sci. Technol.* **2014**, *48*, 3354–3362. [CrossRef]
44. Chen, X.; Su, J.; Meng, Y.; Yu, M.; Zheng, M.; Sun, Y.; Xi, B. Oxygen vacancy promoted heterogeneous Fenton-like degradation of sulfamethazine by chlorine-incorporated micro zero-valent iron. *Chem. Eng. J.* **2023**, *463*, 142360. [CrossRef]
45. Deng, Y.; Tian, X.; Shen, G.; Gao, Y.; Lin, C.; Ling, L.; Cheng, F.; Liao, S.; Zhang, S. Coupling hollow Fe_3O_4 nanoparticles with oxygen vacancy on mesoporous carbon as a high-efficiency ORR electrocatalyst for Zn-air battery. *J. Colloid Interface Sci.* **2020**, *567*, 410–418. [CrossRef]
46. Li, H.; Shang, J.; Yang, Z.; Shen, W.; Ai, Z.; Zhang, L. Oxygen vacancy associated surface Fenton chemistry: Surface structure dependent hydroxyl radicals generation and substrate dependent reactivity. *Environ. Sci. Technol.* **2017**, *51*, 5685–5694. [CrossRef] [PubMed]
47. Ruiz Puigdollers, A.; Schlexer, P.; Tosoni, S.; Pacchioni, G. Increasing Oxide Reducibility: The role of metal/oxide Interfaces in the formation of oxygen vacancies. *ACS Catal.* **2017**, *7*, 6493–6513. [CrossRef]